

GNSS Carrier Phase Improvement Using a MEMS INS-Aided Long Coherent Architecture for High Precision Navigation

Tisheng Zhang¹, Xin Feng¹, Xiaoji Niu¹, Mohamed Bochkati²,
Thomas Pany², *Senior Member, IEEE*, and Jingnan Liu¹

Abstract—The carrier phase measurements of the global navigation satellite system (GNSS) exhibit degraded accuracy and availability in challenging environments, thereby hindering their effective use for intelligent transportation applications. In this paper, an inertial navigation system (INS) aided GNSS signal tracking architecture with long coherent integration periods is proposed to provide accurate and continuous carrier phase observations in challenging environments. In order to implement efficient long coherent integration, a GNSS real time kinematic (RTK)/INS ultra-tight integration algorithm is designed to compensate for the dynamics induced by the receiver-satellite relative motion, and a multichannel cooperative loop with a specialized discriminator is proposed to eliminate the negative effects due to the receiver oscillator instability. Meanwhile, an accurate open loop tracking strategy is designed to sustain the integer ambiguity during a signal blockage, improving the continuity of the carrier phases. Initial blockage test shows that the open loop strategy can keep the carrier phase error below 90 degrees for over 40 seconds. Moreover, an INS based cumulative cycle slip decision variable (CCSDV) is proposed to detect the carrier phase cycle slips accurately. Finally, field vehicle tests were carried out using a (micro-electro-mechanical system) MEMS IMU. It turns out the proposed architecture significantly improves the accuracy and continuity of the carrier phase observations and it can provide superior positioning performance with a small amount of GNSS single frequency observations and a long RTK baseline.

Index Terms—Carrier phase, cycle slips, GNSS/INS, long coherent integration, open loop tracking, ultra-tight integration.

I. INTRODUCTION

CONTINUOUS high-precision absolute positioning plays a crucial role in intelligent transportation applications,

Manuscript received 27 August 2023; revised 22 February 2024 and 5 May 2024; accepted 28 July 2024. This work was supported in part by the National Key Research and Development Program of China under Grant 2020YFB0505803 and in part by the National Natural Science Foundation of China under Grant 41974024. The Associate Editor for this article was Z. M. Kassas. (*Corresponding author: Xiaoji Niu.*)

Tisheng Zhang and Xiaoji Niu are with the Integrated and Intelligent Navigation (I2Nav) Group, GNSS Research Center, Wuhan University, Wuhan 430072, China (e-mail: xjniu@whu.edu.cn).

Xin Feng is with the School of Geodesy and Geomatics, Wuhan University, Wuhan 430079, China.

Mohamed Bochkati and Thomas Pany are with the Institute of Space Technology and Space Applications (ISTA), Universität der Bundeswehr München, 85579 Neubiberg, Germany.

Jingnan Liu is with the GNSS Research Center, Wuhan University, Wuhan 430072, China, and also with the School of Geodesy and Geomatics, Wuhan University, Wuhan 430079, China.

Digital Object Identifier 10.1109/TITS.2024.3436526

such as autonomous vehicles, train localization, mobile robotics [1], [2]. High-precision positioning technologies, such as Real-time kinematic (RTK) or Precise point (PPP) positioning have been proved to provide centimeter-level positioning results when the integer ambiguities of the GNSS carrier phase observations are resolved. The success of the integer ambiguity resolution is highly dependent on the quality of the carrier phase measurements, which, however, will degrade severely in the GNSS signal-challenged environments, e.g., dense foliage, urban canyons, etc. The emergence of autonomous vehicles underscores the growing significance of a GNSS receiver's ability to deliver continuous and precise carrier phase observations, particularly in challenging environments. [3].

There are two distinct levels of improvement in term of the carrier phase continuity and accuracy. First, by adopting some cycle slip detection algorithms, one can detect and compensate the cycle slips of the carrier phases. Besides the observation level efforts [4], the continuous accurate carrier phase observations require continuous accurate tracking of the GNSS signals. Improving the signal tracking performance is a more radical way to provide high performance GNSS observations in challenged environments. The high precision algorithm can benefit from both ways. Humphreys et al. [5] presented a thorough study of the unaided precise GNSS vehicle positioning in challenging environments. It includes several techniques, such as vector signal tracking, adaptive loop control strategy, high rate multi-frequency multi-constellation observations, and a dense reference network, to produce a superior positioning performance. However, the vector tracking without external aiding is highly dependent on the accuracy of the top-level positioning, and it will be unusable in harsh environments where only a small number of satellites are available. Multi-sensor fusion for intelligent vehicle localization solution is the trend and it can both improve the robustness and relax infrastructure requirements.

In this paper, an enhanced GNSS receiver architecture: inertial navigation system (INS) aided long coherent integration (INS-LCI) architecture, is proposed which takes both the carrier phase signal tracking and observation level improvement into account. Its core is an INS-aided long coherent phase lock loop (PLL) with corresponding techniques which enable the long coherent integration in dynamic, signal-challenged

environments. It also includes an INS-aided cycle slip detection algorithm to fix the cycle slips in situations where the long coherent PLL fails.

Long coherent integration is undoubtedly the most effective way to mitigate most of the signal tracking problems [6]: weak signal, multipath, squaring loss, etc. The prerequisite for effective long coherent integration is that the negative effects of the navigation bit sign transition, receiver clock instability and non-linear satellite-user motion should all be mitigated or eliminated during a coherent integration period [7], [8]. Otherwise there will be no actual improvements with the presence of those interferences.

Mature solutions have been developed to solve the navigation bit sign transition problem. For those new GNSS satellite signals with pilot signals, such as Galileo E5a/b, Beidou B2a/b, long coherent integration can be implemented directly because the pilot signals are not modulated with navigation bits [9]. In terms of the signals with navigation bits (e.g., 20 ms per bit for GPS L1 C/A signals), one can either use bit aiding information of an external network [10] or apply bit estimation algorithms [5]. Among the related works, Ren and Petovello [11] did an excellent work to propose a maximum-likelihood (ML) based bit prediction algorithm and they implemented long coherent integration to improve the quality of the code phase and Doppler. Since the bit sign transition is not our research focus, we adopt an external bit aiding source.

The adverse impact due to the receiver oscillator instability can be eliminated by correlator level double difference [12] or mitigated by estimation methods which use an oscillator phase noise model [13], [14]. An in-phase/quadrature signal (I/Qs) level method is used in the proposed INS-LCI architecture to address the oscillator instability during the long coherent integration. An external multichannel cooperative tracking loop is specifically designed to track the receiver oscillator phase error, enabling the long coherent integration of other satellite channels. More designing details can be found in our previous work [15].

Inertial navigation system (INS) is capable of sensing the dynamics caused by the receiver motion. By integrating the dynamics sensed by the INS into the GNSS receiver tracking loops can make the tracking loops work under quasi-static conditions, which is called the GNSS/INS ultra-tight integration. Earlier researches have shown that the performance of PLLs can be enhanced by various grades of IMUs, ranging from high-cost tactical-grade IMUs to more affordable MEMS IMUs [16], [17]. Pany et al. [18] proposed an ultra-tightly coupled GNSS/INS prototype to realize up to several seconds of integration periods and verified the advantages of long coherent integration. But the prototype shows poor performance in real world tests and only the long coherent integration of the code phase tracking is investigated. Soloviev and Dickman [19] tried to track the carrier phase in an indoor scenario with an INS-aided long coherent integration architecture. They successfully realized long coherent carrier phase tracking with centimeter level residuals but the ultimate position accuracy is at the meter level and demonstrated this with less than 1 minute of tests.

Most previous literature only deals with either the dynamic stress or oscillator instability. For example, [18] and [19] both adopted an oven-stabilized, crystal oscillator (OCXO) to mitigate the adverse impact caused by the receiver oscillator instability. However, if there are no targeted measures, the oscillator phase error will eventually become the major source of error, which makes the long coherent integration unable to accumulate enough signal energy. Other studies either only explore the impact of oscillator instability in static scenarios [20], [21], or just conduct simulation studies of the impact of IMU errors [8]. It is necessary to consider both oscillator instability and dynamic stress to implement effective long coherent integration time.

However, the long coherent integration techniques above can only improve the performance of carrier phases under weak signal strengths. They are incapable of addressing discontinuity of the signals. GNSS signals are frequently blocked entirely by surrounding obstacles, such as buildings, utility poles, billboards. Commercial products, such as u-blox F9K [22], MicroStrain 3DM-GQ7-GNSS/INS [23], etc. usually use loosely or tightly coupled integration to solve the problem, which cannot improve the signal tracking performance. The fragile PLLs can lose track easily even when the signal blockage lasts for a very short time (below one second). Stochastic estimation based methods have been developed to improve the continuity of the carrier phase tracking [24]. However, these methods significantly diverge from the classical GNSS receiver structures. Considering the marginal improvements achieved compared to the substantial alterations made to the receiver structure, it may not be justifiable to implement such extensive modifications. There are also another class of representative algorithms called the open loop (OL) tracking [25], [26], [27]. The main idea is to operate with batches of signal samples. A fast Fourier transform (FFT) based parallel search is conducted first to construct the three-dimensional images of received GNSS signals where the image dimensions are the code shift, Doppler shift, and signal energy. Then a more accurate parameter estimation is conducted to generate the information to control the numerical controlled oscillator (NCO). Although they can improve the sensitivity and continuity of the receiver, they only accelerate the PLL to converge after the signal is blocked, which means cycle slips may have already happened during the blockage interval. We intend to maintain the integer ambiguity as long as possible even when the satellite signal is blocked. We have previously proposed a carrier phase prediction method to realize OL tracking [28]. The method can keep the phase error under a half cycle for about 30 seconds. But it is only tested on simulation data and lacks solid open/closed loop control strategies.

The techniques above try to improve the carrier phase performance at the signal processing level. However, cycle slips could still happen in some extremely complex scenarios. Hence, INS-aided cycle slip detection techniques at the observation processing level are necessary to further improve the carrier phase performance. INS-aided cycle slip detection for high precision positioning algorithms are widely studied. Early works adopted high grade IMUs to detect cycle slips [29], [30].

With the development of the multi-constellation and multi-frequency GNSS, the GNSS observation combination are used to detect the cycle slips [31]. Therefore, the requirement for the grade of IMUs can be relaxed. Du and Gao [32] jointly used a consumer-grade IMU and the combinations of carrier phases to detect the cycle slips for PPP. However, the availability of multi-frequency observations in harsh environments remains a problem. Takasu and Yasuda [33] proposed a simple single-frequency integration scheme of INS/RTK-GPS to suppress the errors caused by cycle slips. However, only the time update step of EKF for RTK-GPS positioning is optimized with the corrected velocity from the INS/GPS integration process. The high positioning accuracy over short intervals of an IMU is not fully exploited. Since the position errors of a stand-alone INS will diverge with time, the errors must not exceed a half cycle during the GNSS positioning interval (usually 1 second for a typical receiver). But most recent low cost MEMS IMUs cannot maintain such an accuracy for 1 second. For that reason, the integration rate of MEMS INS/GNSS should be increased, leading high processing load. An accurate lightweight MEMS INS-aided cycle slip detection method is required to solve the problem.

In this paper, the proposed INS-LCI architecture uses the an ultra-tight GNSS/INS integration algorithm and a multichannel cooperative loop to deal with the dynamic stress and clock errors, respectively, providing solid foundations for the long coherent integration. Moreover, a solid OL carrier phase tracking method in the INS-LCI architecture is designed to improve the continuity of the long coherent carrier phase tracking in complex real signal environments. We also present a lightweight INS-aided cycle slip detection method to further improve the carrier phase quality.

The original contributions of this paper are listed as follows:

- 1) The INS aided long coherent integration tracking architecture is first proposed and implemented, which can separate and process the dynamic stress and oscillator instability errors individually at the signal level, enabling effective long coherent carrier phase tracking.
- 2) An accurate carrier phase open loop tracking strategy is designed to sustain the integer ambiguity during short interval of signal blockages, improving the continuity of long coherent tracking in harsh environments.
- 3) At the observation processing level, we propose an INS aided cycle slip detection algorithm with cumulative decision variable to detect the integer and half cycle slips accurately with MEMS IMUs in harsh environments, which surpasses the sensor grade limit of other conventional methods.

II. METHODOLOGY

An intelligent transportation application example diagram of the INS-aided long coherent integration architecture in signal-challenged environments is shown in Fig. 1. A mixture of multipath, attenuated signals is received by the receiver antenna. Moreover, the signals will be blocked by surrounding obstacles now and then, such as buildings, trees, unity poles. The vehicle is equipped with an IMU and a GNSS receiver.

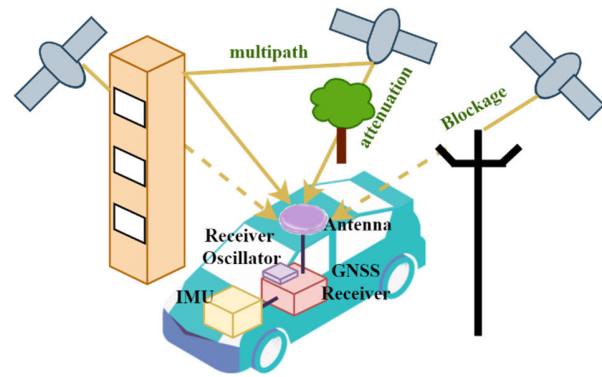


Fig. 1. GNSS signal conditions of vehicles in challenging environments.

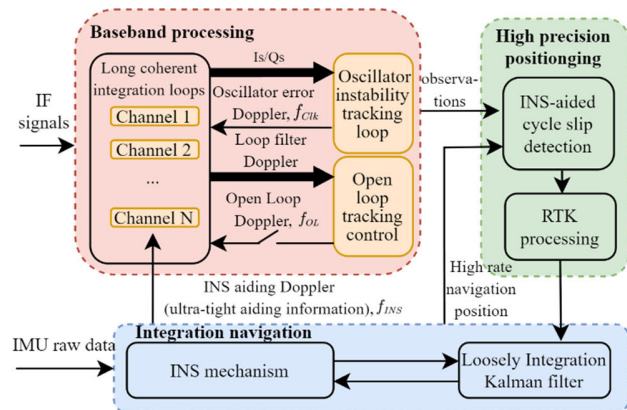


Fig. 2. Overall diagram of INS-LCI architecture.

And the GNSS receiver oscillator is also demonstrated since it's a significant source of error in the long coherent carrier phase tracking.

The technical diagram of the INS-LCI architecture is shown in Fig. 2. Radio frequency (RF) GNSS analog signals are received by the antenna. Then they will be down-converted and digitalized to intermediate frequency (IF) samples by the RF front-end. Multiple channels are incorporated. Each channel tracks a specific satellite's signal.

The goal of the GNSS baseband processing is to generate a replica of the received signal and demodulate the carrier phase and pseudocode. Carrier phase and pseudo-range observations will be extracted during the process. The NCO of the long coherent tracking loop accepts three sources of asynchronous control information, which are the INS aiding Doppler (f_{INS}) generated by INS, the Doppler induced by the oscillator instability (f_{clk}), and the output of the local loop filter (f_{Lop}):

$$f_{NCO} = f_{INS} + f_{clk} + f_{Lop} \quad (1)$$

The INS aiding Doppler is evaluated by projecting the receiver-satellite motion to the line of sight (LOS) direction. It will compensate for the Doppler effect due to LOS relative dynamics between the receiver and the satellite. Ultra-tight GNSS/INS integration leaves the receiver oscillator instability the main source of signal tracking errors, which has the same effect on every channel [34], [35]. We select those channels with strong signal strength and high elevation angles

as the oscillator error estimation channels. Their integrated and dumped in-phase and quadrature signals will be sent to a wideband tracking loop, which is specially designed for the estimation and tracking of the oscillator error. Outputs of the multichannel cooperative oscillator instability tracking loop will be injected to the NCOs of local channels, compensating for the oscillator induced Doppler effect. As a result, only the thermal noise will dominate the signal errors. In this way, the benefits brought by the long coherent integration can be maximized for its capability to vastly increase the signal SNR. Finally, the long coherent integration loop should only track the extreme slow varying dynamic and oscillator error residuals. It's because the bandwidth of the multichannel cooperative loop cannot be infinite wide and the high frequency oscillator phase errors will be sent to the local tracking loops.

As previously mentioned, GNSS signals can be intermittent due to the blockage caused by surrounding building, trees, billboards, etc. So an open/closed tracking strategy is developed to maintain the integer ambiguity of the carrier phase observations under such circumstances. When a degradation of the single power and the phase lock indicator (PLI) is detected, the local loop will switch from the closed to open loop tracking mode. In OL tracking mode, the local loop filter output will be replaced with the OL Doppler to control the NCO. Since the oscillator residual errors are common-mode in different long coherent channels, the OL Doppler will be estimated by integrating loop filter Doppler from other closed mode loops.

Apart from the accurate and robust tracking strategies in GNSS signal tracking, observation level efforts are made to detect the cycle slips. The short-term accuracy of an INS is used to detect the cycle slips. Optimized carrier phases will be sent to a RTK algorithm. The high level loose integration between the RTK GNSS and INS will be implemented in the integration Kalman filter, where the errors of the IMU can be calibrated.

All techniques have been implemented in a software defined GNSS/INS ultra-tight receiver (I2xSNR) developed by the Integrated & Intelligent Navigation (I2Nav) Group. The detailed description of these techniques will be provided below.

A. GNSS/INS Ultra-Tight Integration

The ultra-tight GNSS/INS integration compensates for the receiver-satellite dynamics by assisting the NCO control of local loops with respective INS aiding Doppler. The INS mechanism provides the position and velocity of the receiver, which will be used to calculate the aiding Doppler. Besides, the RTK GNSS is integrated with INS in loosely coupled mode to bind the INS error accumulation. The Doppler caused by the relative motion between the satellite and receiver (user) is composed of two components, which can be expressed as:

$$\begin{aligned} f_{INS} &= f_S^{(i)} + f_U \\ &= \mathbf{I}_{SU}^{(i),e} \left(\frac{v_S^{(i)}}{\lambda} + \frac{-v_U}{\lambda} \right) \end{aligned} \quad (2)$$

where $f_S^{(i)}$ and f_U are the Doppler caused by the motion of the i_{th} satellite and the receiver, respectively. λ denotes the carrier

wavelength. The velocity of the i_{th} satellite ($v_S^{(i)}$) is evaluated through the time and ephemeris, and the INS provides the velocity of the receiver (v_U) with a high frequency. $\mathbf{I}_{SU}^{(i),e}$ denotes the unit vector in the LOS direction between the satellite and receiver. The superscript e means the derivation is conducted in the Earth-centered Earth-fixed (ECEF) reference coordinate system. The unit direction vector $\mathbf{I}_{SU}^{(i),e}$ is calculated by:

$$\mathbf{I}_{SU}^{(i),e} = \frac{\mathbf{P}_S^{(i),e} - \mathbf{P}_U^e}{\|\mathbf{P}_S^{(i),e} - \mathbf{P}_U^e\|} \quad (3)$$

where $\mathbf{P}_S^{(i),e}$ and \mathbf{P}_U^e denote the position of the i_{th} satellite and the receiver.

The update rate of the INS aiding Doppler should be high enough to compensate for the fast varying motion induced dynamics. However, the sampling rate of an IMU varies from tens to hundreds of hertz, which is not sufficient especially when a low IMU sampling rate is adopted. Considering the fact that the dynamics of a vehicle are small, a linear extrapolation is sufficient to fill the gap between two successive IMU samples. The linear extrapolation is based on the assumption that the acceleration remains constant in an INS update interval. Assume the sampling rate of the IMU is T_I , and the extrapolation of the receiver motion induced Doppler is expressed as:

$$f_U(kT_I + \Delta t) = f_U(kT_I) - \mathbf{I}_{SU}^{(i),e} \cdot \frac{a_U(k|T_I)}{\lambda} \cdot (\Delta t) \quad (4)$$

where k denotes the k_{th} IMU sample, and $a_U(k|T_I)$ denotes the acceleration of the IMU.

The high rate satellite motion induced Doppler can be extrapolated in a similar manner:

$$f_S(kT_P + \Delta t) = f_S(kT_P) + \frac{f_S(kT_P) - f_S((k-1)T_P)}{T_P} \cdot \Delta t \quad (5)$$

where the T_P is the update period of the positioning (typically 1 s). The motion of a satellite can be considered as uniform acceleration during a positioning update interval, and the change of the LOS direction vector is small enough to be neglected.

The ultra-tight integration in this work employs a low cost MEMS IMU to compensate for the satellite-receiver motion induced dynamics. The INS aiding Doppler is updated with a frequency of 1000Hz to guarantee the effectiveness of the ultra-tight integration. It is note that the performance of GNSS/INS ultra-tight integration may vary when different types of IMUs are used. The quantitative analysis to the impacts of IMU quality in GNSS/INS ultra-tight integration can be referred to [36].

B. Multichannel Cooperative Oscillator Instability Tracking

The diagram of the multichannel cooperative LCI tracking loop is shown in Fig. 3. After carrier mixing and code correlation, the carrier and code signals are stripped from the received GNSS signals, leaving the pre-detection in-phase and quadrature signals. Integration and dump will be conducted

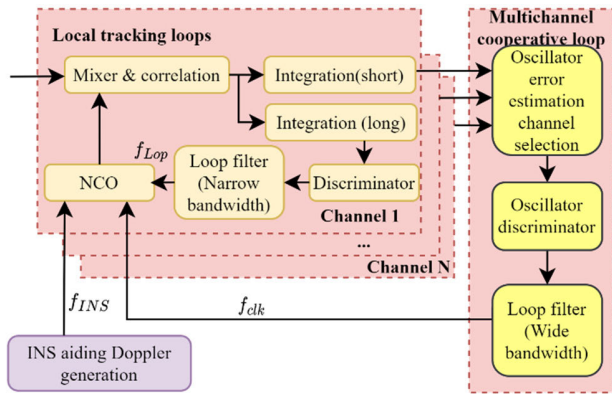


Fig. 3. Diagram of multichannel cooperative LCI loop.

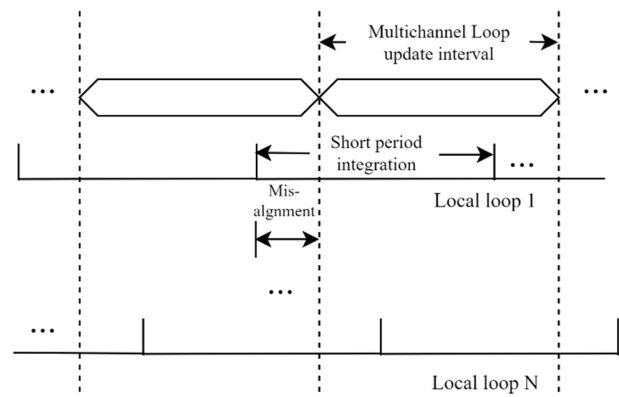


Fig. 4. Asynchronous update of different channels.

right after the carrier and code wipe-off processes. The integrated pre-detection signals are given by:

$$\begin{aligned} I(n) &= D(n) \text{sinc}(f_e T) \cos(\theta_e) \\ Q(n) &= D(n) \text{sinc}(f_e T) \sin(\theta_e) \end{aligned} \quad (6)$$

where the $I(\cdot)$ and $Q(\cdot)$ represent the in-phase and quadrature signal component, respectively. $D(\cdot)$ denotes the navigation bit value. f_e and θ_e denote the average frequency and phase error during the integration interval.

Two different periods of integration will be conducted. The short period integrated pre-detection signals of all local loops will be sent to the wide-band multichannel cooperative loop which is designed to track the common-mode oscillator phase error. And the local loop will adopt a long coherent integration period and narrow loop bandwidth to suppress the thermal noise.

A channel selection strategy is designed first to screen out those channels with low carrier-to-noise-ratio (C/N_0) values and low satellite elevation angles. Then an oscillator error discriminator is used to estimate the phase error induced by the oscillator instability. Assume the short integration period is T_{Clk} and M channels are selected from N local channels. The discriminator can be expressed as:

$$\tilde{\theta}_c = \frac{\sum_{i=1}^M I_{Clk}^{(i)} \cdot Q_{Clk}^{(i)}}{\sum_{i=1}^M (I_{Clk}^{(i)})^2} \quad (7)$$

where the subscript $(\cdot)_{Clk}$ indicates the short period integrated pre-detection signals which are used to estimate the clock phase errors ($\tilde{\theta}_c$). The clock phase error estimate is sent to a wide bandwidth filter to generate the oscillator error Doppler, which will be used to control the local NCOs.

It is worth noting that the short time update periods of different local channels do not align perfectly. In other words, as shown in Fig. 4, the I_s and Q_s in (7) arrive at different moments of time. Since the drifting of the receiver clock varies slowly, the misalignment will pose no significant delays. Nevertheless, the integration period can be shortened to mitigate the impact cause by the delays. If the integration with the length equal to the correlator's (e.g. 1 ms for GPS L1), is adopted, the delay will be zero. But the tracking noise will

be relatively high. Hence there is this tradeoff between the oscillator error Doppler delay and noise suppression.

C. Long Coherent Integration

As shown in Fig. 3, the local loop performs a long coherent integration tracking with the pre-requisite that the motion induced dynamics and oscillator errors are compensated. In general, the integration period longer than 100 ms is considered as long coherent integration [15]. After bit synchronization, the local loop will perform a fundamental integration of the length equivalent to a navigation bit (e.g. 20 ms for GPS L1), which is written as:

$$\begin{aligned} I_B &= D(n) \text{sinc}(f_e(n) T_B) \cos(\theta_e(n)) \\ Q_B &= D(n) \text{sinc}(f_e(n) T_B) \sin(\theta_e(n)) \end{aligned} \quad (8)$$

where T_B is the length of a navigation bit.

Then, the long coherent integration is implemented by accumulating N_L successive epochs of the fundamental integrated pre-detection signals:

$$\begin{aligned} I_L &= \sum_{n=1}^{N_L} \tilde{D}(n) I_B(n) \\ Q_L &= \sum_{n=1}^{N_L} \tilde{D}(n) Q_B(n) \end{aligned} \quad (9)$$

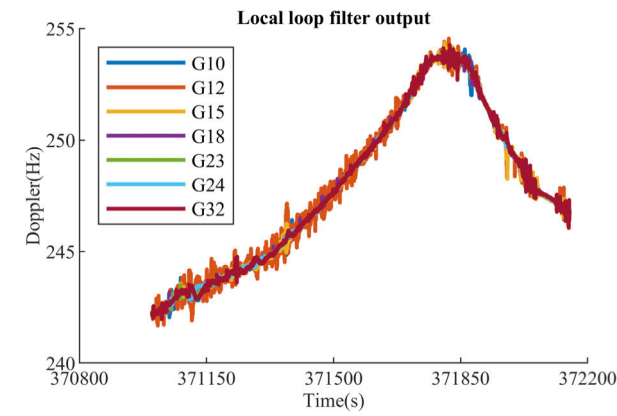
where $\tilde{D}(n)$ is the n_{th} external aiding bit value.

The long coherent integrated I and Q path signals will be sent to the local discriminator and then the loop filter. Outputs of the loop filter (f_{Lop}) are used to control the loop NCO to realize the long coherent closed loop tracking.

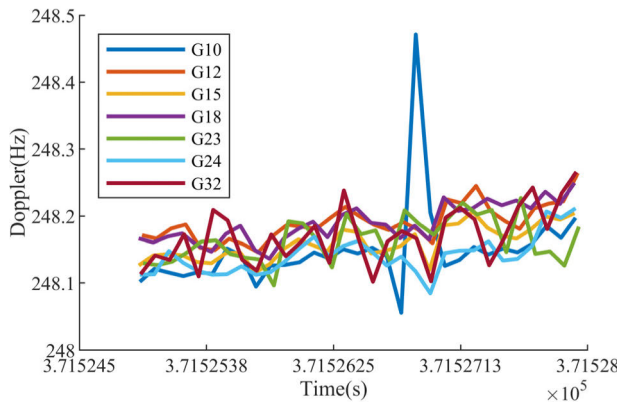
By all accounts, the INS aiding Doppler (f_{INS}), oscillator error Doppler (f_{Clk}) and local loop filter output (f_{Lop}) control the local NCO asynchronously, enabling accurate and robust long coherent carrier phase tracking.

D. Accurate Carrier Phase Open Loop Tracking

As the bandwidth of the multichannel cooperative loop cannot be infinite, the residuals of the high frequency oscillator tracking error will be left for the local loops to process. Fig. 5 shows the output Doppler of the local loop filters when ultra-tight integration and the multichannel cooperative loop is adopted. The long term trend is shown in the upper



(a) Long term trend



(b) Magnified view of (a)

Fig. 5. Doppler of the oscillator tracking error residuals.

sub-figure (a). On one hand, the Doppler varies very slowly because of the accumulation effect of the local filter. On the other hand, although the noise levels of different channels differ from each other, the long term trends are highly consistent, which can be used to realize the accurate open loop tracking. Fig. 5 (b) is the enlarged version of (a) in the period from 371525s to 371528s. The biases of different local channels are slightly different with each other. The reason for this phenomenon is that the motion induced dynamic residuals and the propagation errors are different across different channels.

Fig. 6 demonstrates the diagram of the accurate carrier phase open loop tracking. The pre-processing module is the collection of the signal processing components mentioned above, including the mixer, correlator, integration and phase discriminator. The closed loop tracking channels with high C/N_0 and PLI values will be selected, whose loop filter Doppler outputs will be sent to a smoother. After smoothing, the slow varying long term trend ($f_{Lop,Smo}^{(i)}$) and rapid varying jitter ($f_{Lop,Jit}^{(i)}$) of the i_{th} channel loop filter Doppler can be separated:

$$f_{Lop}^{(i)} = f_{Lop,Smo}^{(i)} + f_{Lop,Jit}^{(i)} \quad (10)$$

However, the smoothed Doppler of different channels do not share a same bias. So the increment between two successive

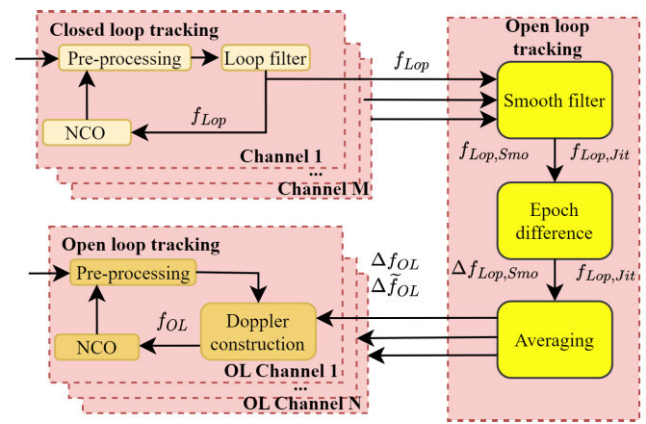


Fig. 6. Diagram of the accurate open loop tracking.

epochs is evaluated:

$$\Delta f_{Lop,Smo}^{(i)}(n) = f_{Lop,Smo}^{(i)}(n) - f_{Lop,Smo}^{(i)}(n-1) \quad (11)$$

Then the average of the increments from different channels is evaluated:

$$\Delta f_{OL}(n) = \frac{1}{M} \sum_{i=1}^M \Delta f_{Lop,Smo}^{(i)}(n) \quad (12)$$

Besides, the jitter average ($\Delta \tilde{f}_{OL}$) will also be evaluated:

$$\Delta \tilde{f}_{OL}(n) = \frac{1}{M} \sum_{i=1}^M f_{Lop,Jit}^{(i)}(n) \quad (13)$$

Both the increment and jitter will be used to construct the open loop control Doppler.

The open loop control Doppler construction is based on an incremental model. Assume the open loop tracking starts at time 0, and the n_{th} open loop control Doppler ($f_{OL}(k)$) can be written as:

$$f_{OL}(n) = f_{OL}(0) + \sum_{j=0}^n \Delta f_{OL}(j) + \Delta \tilde{f}_{OL}(n) \quad (14)$$

where $f_{OL}(0)$ is the initial open loop Doppler at the starting point.

It is worth noting that different channels do not update synchronously. There are temporal delays in the open loop increment and jitter Doppler. Nonetheless, as shown in Fig. 4 (b), the short term variation of the oscillator residual error induced Doppler can be considered as linear. The delays can be neglected.

The open-closed loop switch strategy is vital for the continuity of the carrier phase tracking. Fig. 7 shows the finite state machine of the open-closed loop switch strategy. Two factors are taken into consideration when determining whether to perform open or closed loop tracking. One is the PLI value (P_{PLI}), and the other is the signal energy level (P_{Eng}). Of course, C/N_0 value is a metric to indicate the signal power. But its update rate is low, which cannot sense the signal power variation in time. Besides, the C/N_0 measurement noise will increase as the loop tracking performance deteriorates.

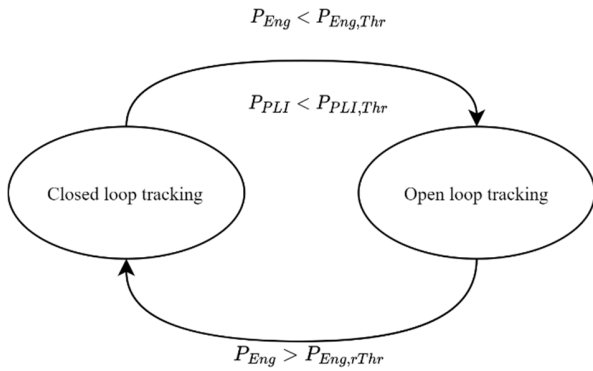


Fig. 7. Finite state machine of the open/closed tracking strategy.

As a result, C/N_0 value is not suitable as the indicator in open-closed loop tracking switching.

The PLI value of a PLL is defined as:

$$P_{PLI} = \frac{I^2 - Q^2}{I^2 + Q^2} \quad (15)$$

It reflects the energy distribution across I and Q signal paths. PLI varies between -1 and 1 . The closer the PLI value is to 1 , the more accurate the tracking is. PLI itself is insufficient to indicate the availability of the signal. The dimension of signal energy is necessary.

The energy of an integrated pre-detection signal is defined as:

$$E = I^2 + Q^2 \quad (16)$$

Since the absolute signal energy varies with different integration periods, it should be normalized by an energy benchmark (E_B). The energy benchmark is derived by calculating the moving average of the absolute energy. Only when the PLL is tracking the carrier phase stably (with high PLI values), the effective absolute energy values will be used to calculate the energy benchmark. Then normalized signal energy is denoted as:

$$P_{Eng} = \frac{E}{E_b} \quad (17)$$

The normalized signal energy reflects the existence of signal energy and the PLI reflects the distribution of energy between the I and Q path. Both of them are necessary for efficient open/closed loop tracking switching. As shown in Fig. 7, when both P_{PLI} and P_{Eng} are smaller than the thresholds ($P_{PLI,Thr}$ and $P_{Eng,Thr}$, respectively), the signal will be considered as blocked and the local loop will switch from the closed to open loop tracking mode. As the satellite becomes visible again, a rise of P_{Eng} will be observed. When it exceeds the recovery threshold ($P_{Eng,rThr}$), the local loop will return to the closed tracking mode.

E. INS-Aided Cycle Slip Detection With Cumulative Decision Variable

The cycle slip decision value (DV) is derived through a three-step differencing process. First, the time difference of the carrier phase observations and INS estimated satellite-receiver

ranges is computed. Afterwards, the difference between these time-differenced results is calculated. Finally, a reference satellite is selected, and the difference between the first two-step differencing results of the reference satellite and those of the other satellites is determined.

The diagram of the INS-aided cycle slip detection is shown in Fig. 8. The estimate of the satellite-receiver range will be derived through the INS solution and ephemeris in the first place:

$$\hat{r}^{(i)} = \|\mathbf{P}_S^{(i),e} - \mathbf{P}_U^e\| \quad (18)$$

The carrier phase is defined as:

$$\phi^{(i)} = r^{(i)} + c \cdot \delta t_u - c \cdot \delta t^{(i)} - I^{(i)} + T^{(i)} + N^{(i)} + \varepsilon^{(i)} \quad (19)$$

where $r^{(i)}$ is the absolute range between the satellite and receiver. δt_u and $\delta t^{(i)}$ denote the receiver and satellite clock error, respectively. $I^{(i)}$ and $T^{(i)}$ are the ionosphere and troposphere propagation errors, respectively. c denotes the light speed. $N^{(i)}$ is the integer ambiguity. The stochastic noise is denoted as $\varepsilon^{(i)}$. The time differenced carrier phase is denoted as:

$$\begin{aligned} \Delta\phi^{(i)} &= \Delta r^{(i)} + c \cdot \Delta\delta t_u - c \cdot \Delta\delta t^{(i)} \\ &+ \Delta T^{(i)} - \Delta I^{(i)} + \Delta N^{(i)} + \Delta\varepsilon^{(i)} \end{aligned} \quad (20)$$

Since the sampling rate of carrier phases is generally larger than 1Hz and the propagation errors vary very slowly between two successive epochs [37], their epoch differences can be assumed 0. Moreover, the epoch difference of the satellite clock error is assumed 0 as an atomic clock is equipped. It is noted that the antenna phase center error and multipath effect are ignored in (19) to avoid verbosity. The antenna phase error is neglectable after time difference, and the long coherent integration tracking has mitigated the multipath significantly. Then (20) is written as:

$$\Delta\phi^{(i)} = \Delta r^{(i)} + c \cdot \Delta\delta t_u + \Delta N^{(i)} + \Delta\varepsilon^{(i)} \quad (21)$$

The epoch differenced satellite-receiver range estimation through the INS can be regarded as a pseudo-station. The result of the station-difference is expressed as:

$$\begin{aligned} \Delta\Phi^{(i)} &= \Delta\phi^{(i)} - \Delta\hat{r}^{(i)} \\ &= \nabla\Delta r^{(i)} + c \cdot \Delta\delta t_u + \Delta N^{(i)} + \Delta\varepsilon^{(i)} \end{aligned} \quad (22)$$

where $\nabla\Delta r^{(i)} = [r_k^{(i)} - \hat{r}_k^{(i)}] - [r_{k-1}^{(i)} - \hat{r}_{k-1}^{(i)}]$ is the range estimation error of the k_{th} and $(k-1)_{th}$ epoch, which is highly related to the INS short term accuracy.

The satellite difference is performed to eliminate the receiver clock error:

$$\Delta\Phi^{(i,k)} = \Delta\Phi^{(i)} - \Delta\Phi^{(k)} = \nabla\Delta r^{(i,k)} + \Delta N^{(i,k)} + \Delta\varepsilon^{(i,k)} \quad (23)$$

A channel with its carrier phase stably tracked will be chosen as the reference channel. If the integer ambiguity remains constant during the detection interval, $\Delta N^{(i,k)}$ would be 0. Although the INS/RTK integration provides a centimeter level

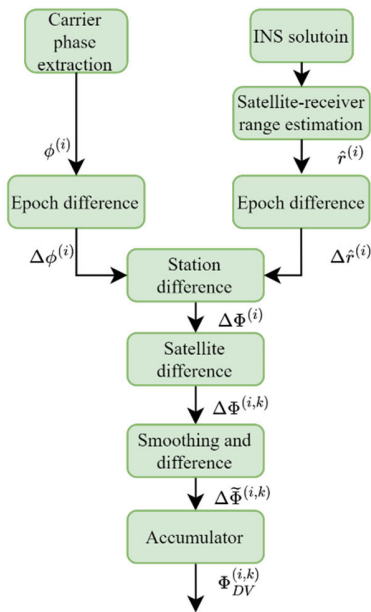


Fig. 8. Diagram of the INS-aided cycle slip detection.

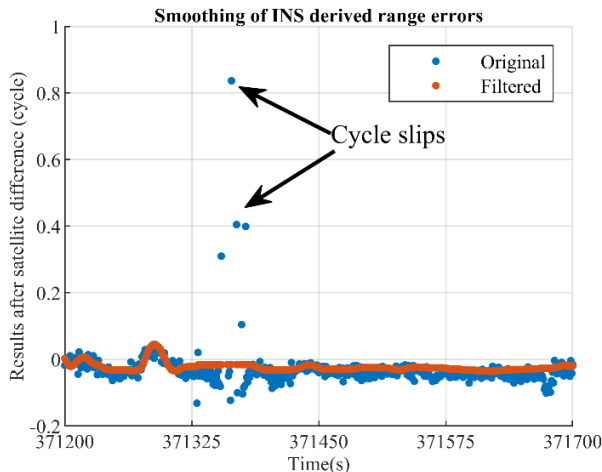


Fig. 9. Smoothing of the INS derived range errors.

positioning accuracy, the INS derived range error would still make the curve of $\Delta\Phi^{(i,k)}$ to fluctuate with a small amplitude. So the results after the satellite difference is sent to a smoother. Then the difference between the results before and after the smooth filtering will be evaluated as the raw cycle slip decision variable (DV):

$$\Delta\tilde{\Phi}^{(i,k)} = \Delta\Phi^{(i,k)} - \Delta\Phi_{Smo}^{(i,k)} \quad (24)$$

where $\Delta\Phi_{Smo}^{(i,k)}$ denotes the filtered data. The filtering process is shown in Fig. 9 where a tactical grade IMU is adopted. The difference shown in (24) will eliminate the effect of the fluctuation, leaving the noise following the Gaussian distribution with its mean value equal to 0. Those gross errors are the detected cycle slips, including both the integer and half cycle slips.

Conventional INS-aided cycle slip detection methods just use the raw cycle slip decision variable. As a result, the success of the cycle slip detection is highly depended on the

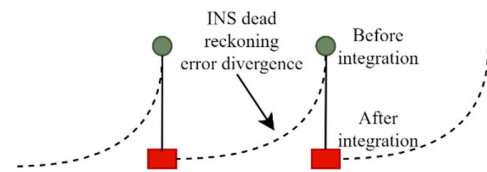


Fig. 10. INS dead reckoning error divergence.

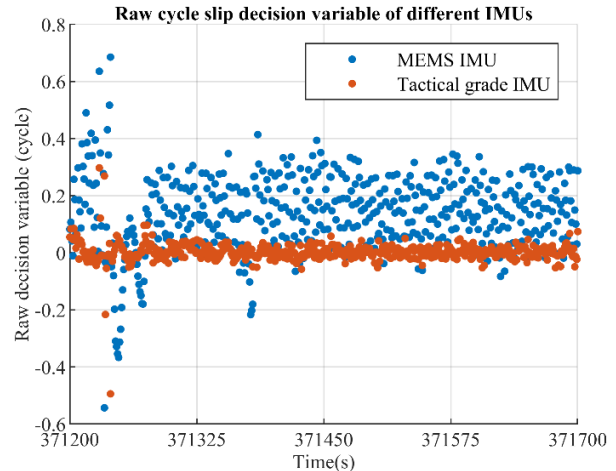


Fig. 11. Raw cycle slip decision variables of different grades of IMUs.

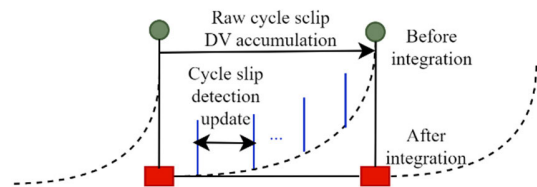


Fig. 12. Derivation of the accumulated cycle slip decision variable (ACSDV).

accuracy of the INS dead reckoning. Fig. 10 shows the process of the INS/RTK integration. The INS dead reckoning error will diverge between two positioning epochs (generally 1 s). In order to detect the cycle slips correctly, the error divergence must be contained far below half a carrier phase cycle, which restricts the grade of the selected IMU significantly.

The Raw cycle slip decision variable of different grades of IMUs is shown in Fig. 11. Compared with the tactical grade IMU, the relative positioning error of a MEMS IMU between two positioning epochs is much larger. So the raw DV error of the MEMS IMU greatly exceeds that of the tactical grade IMU. Moreover, the MEMS IMU raw DV error amplitude is very close to half a cycle, which will cause a significant performance deterioration of the cycle slip detection algorithm.

An intuitive solution for the problem is to increase the update rate of the RTK positioning and INS/RTK integration so that the error of the IMU can be calibrated in time. But this solution will bring extreme high processing load, which is not economical.

We propose the cumulative cycle slip decision variable (CCSDV) to solve the problem. Instead of increasing the positioning rate, we only increase the rate of the carrier phase extraction. In addition, the INS solution will be extrapolated to align with the carrier phase extraction moment. Then the



Fig. 13. Trajectory of the field test.

cycle slip detection will be performed. In this way, the long period between two positioning epochs is divided into many short term intervals. Even low cost MEMS IMUs are capable of suppressing the dead reckoning errors far below half a cycle during those short intervals. At last, the raw cycles slip DVs of these short intervals will be accumulated to construct the final decision variable:

$$\Delta\Phi_{DV}^{(i,k)} = \sum_{j=1}^{N_{CS}} \Delta\tilde{\Phi}^{(i,k)}(j) \quad (25)$$

where N_{CS} is the number of cycle slip detections during a positioning period. It's the ratio between the cycle slip detection rate (f_{CS}) and the positioning (f_{Pos}) rate ($N_{CS} = f_{CS}/f_{Pos}$). Finally, the ACS DVs will be used to detect and identify the cycle slips. It is noted that the cycle slip detection rate should be adjusted (f_{CS}) according to the grade of the IMU to guarantee the accuracy of the detection result.

The cycle slip detection is conducted first. It determines whether cycle slips have occurred or not. If the absolute value of an ACS DV exceeds a predefined detection threshold ($|\Delta\Phi_{DV}^{(i,k)}| > T_{CS_D}$), cycle slips are determined as detected. Then a cycle slip identification is conducted. It identifies the exact number of slipped cycles. Since the local carrier phase tracking loops are Costas loops whose pull-in phase errors are between -90° and $+90^\circ$, it is very likely that a small interference will cause the tracking loops to generate a carrier phase observation with half cycle slips. As a result, both the integer and half cycle slips are identified:

$$m/2 - T_{CS_I} < \Delta\Phi_{DV}^{(i,k)} < m/2 + T_{CS_I} \quad (26)$$

where the T_{CS_I} denotes the threshold of the cycle slip identification, and $m/2, m = \dots, -1, 0, +1, \dots$ is the number of slipped cycles.

The thresholds are set according to the testing probabilities of this method, which include the false alarm, missed detection, right identification and false identification:

$$P_{FA} = 2\text{erfc}\left(\frac{T_{CS_D}}{\sigma}\right)$$

$$P_{MD} = \text{erfc}\left(\frac{m - T_{CS_D}}{\sigma}\right) - \text{erfc}\left(\frac{m + T_{CS_D}}{\sigma}\right)$$

$$P_{RD} = 2\text{erf}\left(\frac{T_{CS_I}}{\sigma}\right) - 1$$

$$P_{FD} = 2 \sum_{i=1}^{\infty} \left\{ \text{erf}\left(\frac{i/2 + T_{CS_I}}{\sigma}\right) - \text{erf}\left(\frac{i/2 - T_{CS_I}}{\sigma}\right) \right\} \Big|_{i \neq m} \quad (27)$$

where the σ is the standard deviation of the ACS DV, and $\text{erf}(x) = \frac{2}{\sqrt{\pi}} \int_0^x e^{-t^2} dt$. More details can be referred to [38].

The cycle slips will be compensated for if the exact number of slipped cycles is identified. A compensation register is used to store the slipped cycles since the beginning of the detection. Every time a carrier phase observation is generated the value of the register will be added to the carrier phase to maintain the integer ambiguity. If otherwise the cycle slips are detected but the identification fails, the carrier phase will be removed from the positioning. Besides, the cycle slip compensation register will be cleared and the integer ambiguity will be re-evaluated by the positioning algorithm.

III. EXPERIMENT SETUP

In order to test the performance of the INS-LCI architecture, a field vehicle test is conducted in an industrial area in Wuhan China. The trajectory is shown in Fig. 13. The reason for selecting this testing field is that this area contains typical scenarios which cover the signal strength degradation caused by foliage, the blockage of buildings and utility poles, etc. In addition, as shown in Fig. 14, only one or two negative factors appear at one time, which is helpful and convenient for us to analyze the performance of the proposed techniques specifically.

The test was conducted on the GPS L1 signals, which is sufficiently challenging due to the shortage of available satellites. The satellite distribution is shown in Fig. 15. Four of the seven satellites' elevation angles were below 45° , which requires robust and accurate tracking of those satellites to sustain continuous accurate RTK solutions.

A static rooftop GNSS receiver was set 13 kilometers away from the testing field to provide the reference observations for the RTK algorithm. The testing vehicle is shown in Fig. 16. The test equipment was installed on top of and inside the car. The GNSS signals are received by a common antenna and then distributed by a splitter. A high precision Position and Orientation system (POS), Ledor PPOI-A15 is adopted as the reference system. It is composed of a multi-constellation multi-frequency GNSS receiver and a ring laser gyro IMU. The post-process navigation results of Ledor A15 are served as the ground truth.

The GNSS IF signals are recorded by the Spirent GNSS signal record and playback systems GSS6450 [39]. A low cost GNSS/INS integration module developed by I2Nav Group, INS-Probe, is used to record the data of a MEMS IMU, ADIS 16465. The recording of the IMU data is synchronized to the GPS time. In addition, the observations of a commercial GNSS receiver, Ublox F9P [40] are also recorded by the INS-Probe for a comparison. The software defined GNSS receiver I2xSNR is used to process the IF signals and the



(a) Forliages and utility poles



(b) Buildings

Fig. 14. Test scenes during the field test.

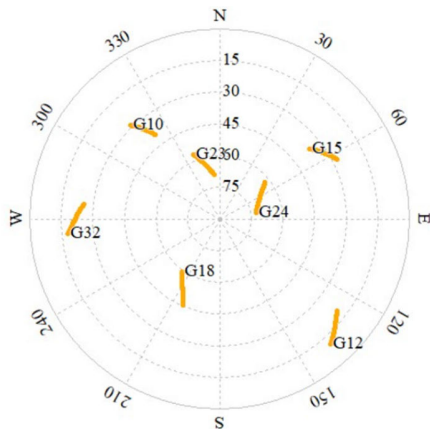


Fig. 15. Satellite distribution of the experiment.

data of the testing IMUs. Specific parameters of the IMUs adopted in this experiment are shown in TABLE I. Leader A15 is equipped with a typical tactical grade IMU and the ADIS 16465 is commercial grade.

Different levels of performance tests will be conducted in the following section. It is noted that although only the GPS L1 signals are processed for the performance tests, the INS-LCI architecture can be used to process the signals of different frequencies from different constellations.

IV. RESULTS AND DISCUSSION

The multichannel cooperative loop has been tested thoroughly in our previous work [15]. Hence, focusing on the long coherent carrier phase tracking in complex dynamic environments, this section presents specific tests on the techniques



(a) Testing vehicle



(b) Equipment on top



(c) Equipment inside

Fig. 16. Test vehicle and equipment.

TABLE I
PARAMETERS OF THE TESTING IMUS

Parameters	Leader A15	ADIS 16465
Gyroscope angular random walk (deg/sqrt(hr))	0.003	0.1
Gyroscope bias instability (deg/hr)	0.027	50
Accelerometer velocity random walk (m/s/sqrt(hr))	0.03	0.1
Accelerometer bias instability (mGal)	15	50

including GNSS/INS ultra-tight integration, long coherent tracking, open loop tracking and INS-aided cycle slip detection. First, two signal tracking level tests will be conducted. One is performed to explore the benefits of different grades of IMUs for the long coherent integration. The other is an open loop test with the aim to evaluate its ability to preserve the carrier phase integer ambiguity. After that, the

observation level test is conducted to verify the validity and performance of the INS-aided cycle slip detection algorithm. Finally, a synthetic test is conducted to present an overall performance evaluation of the INS-LCI architecture.

A. Effects of Different Grades of IMUs for the Long Coherent Integration

As mentioned before, the ultra-tight INS/GNSS integration eliminates most of the dynamics induced by the receiver-satellite motion, leaving only the dynamic residuals for local loops to track. Higher grades of IMUs leave lower residuals, which means longer coherent integration period can be achieved. In this test, the oscillator instability will be eliminated by the multipath cooperative loop, based on which the power of the integrated signals using different IMUs will be compared.

Fig. 17 shows the signal power with 100 ms coherent integration period using the Ledor A15 IMU and ADIS 16465. Three satellites with the PRN 12, 18 and 23 are tested and they have low, medium and high elevation angles respectively. Since the GNSS signals are processed by digital channels, the magnitude of the integration and dump output will be calculated as the signal power directly, which has no physical unit. Satellite GPS 12 has the lowest absolute signal power level due to its low elevation angle. The two curves of different IMUs for each satellite are highly consistent with each other. The signal power with 100 ms coherent integration period of the Ledor A15 IMU and ADIS 16465 is very close to each other, so it seems the red curve “completely covers” the blue curve. This indicates that both IMUs can deal with the dynamic stress when 100 ms of integration period is adopted.

As the coherent integration period increases, the accumulated INS errors will have a negative impact on the integrated signal power. Fig. 18 demonstrates the phenomenon. When 200 ms of integration period is adopted, the Ledor A15 IMU can still sustain the effective power accumulation. But the INS errors of ADIS 16465 hinder the effective accumulation of energy in the long coherent integration.

The test results indicate that higher grades of IMUs are more beneficial to the long coherent integration. Despite this, a MEMS IMU is still capable of supporting the coherent integration period up to 100 ms for carrier phase in the prerequisite that the oscillator error is eliminated first. The low cost ADIS 16465 IMU will be used in the following tests, which is suitable for the mass market applications.

B. Effective Time of Open Loop Tracking

The carrier phase open loop tracking strategy is designed to sustain the integer ambiguity when the GNSS signal is not available for a short period. In this test, the effective time of the open loop tracking will be explored. By “effective”, we mean the phase error cannot exceed a quarter cycle. In order to evaluate the effective time quantitatively, a channel with strong signal strength is selected as the testing open loop channel. Its local loop filter output will be replaced with the OL Doppler, and the phase discriminator result can accurately reflect the phase tracking error. Since the local NCO control information

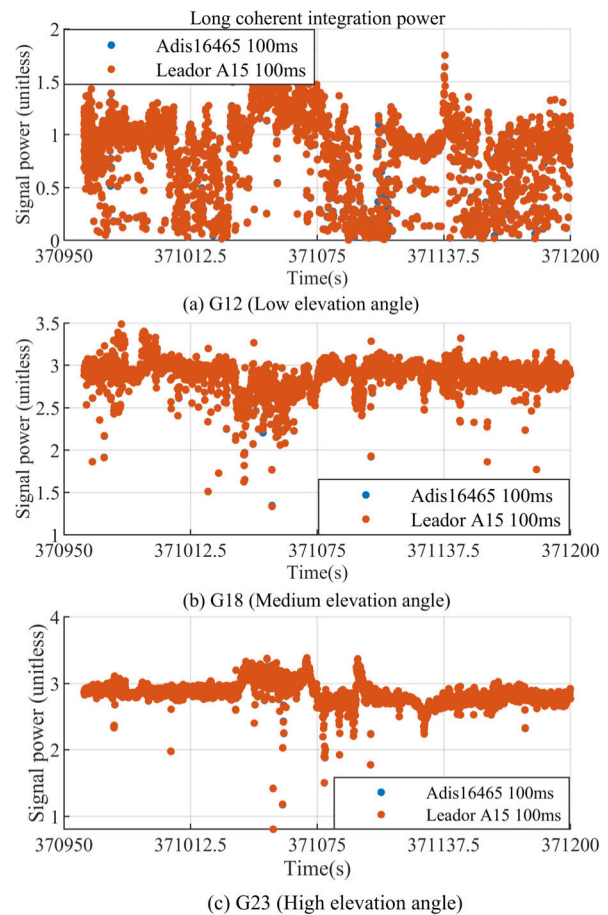


Fig. 17. Signal power with 100 ms of coherent integration period.

of the open loop channel is derived from other channels, the unique errors of the channel, such as the atmospheric delay, cannot be tracked accurately. Hence, the error of the open loop carrier phase will diverge with time. The period from the OL start moment to when the discriminator error exceeds 90 degrees will be considered as the effective OL time.

The ADIS 16465 is used to estimate the dynamic stress and the multichannel cooperative loop tracks the oscillator phase error. These local loops perform 100 ms coherent integration periods. Fig. 19 shows the test result of satellite GPS 23. The blue and red curves represent the closed and open tracking modes respectively. The local loop of GPS 23 switches to open loop tracking mode at 371297s and the phase error exceeds a quarter cycle at 371343s. So the effective time is 46 seconds, which are enough for a vehicle to pass through an overpass, a billboard, a building, etc.

The initial test above proves that the accurate open loop tracking strategy solves the problem that the carrier phase integer ambiguity of the satellite has to be re-estimated when a short interval of signal blockage happens. When a longer coherent integration period is adopted, the narrower bandwidth should be used to realize stable signal tracking, which makes the OL strategy more significant. The OL carrier phase observations will not be used in the positioning algorithm generally because the NCO control information of an OL channel is derived from other closed loop channels. However, if there

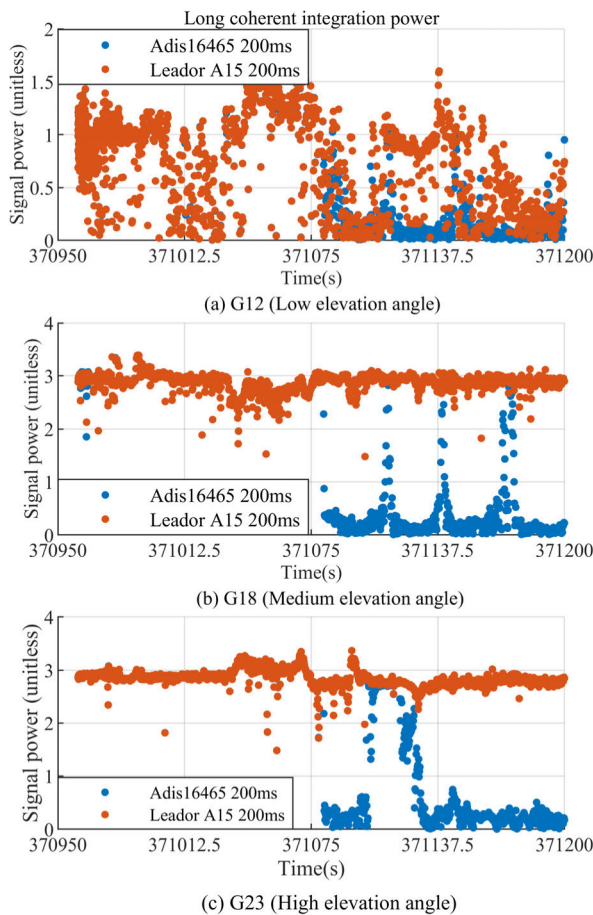


Fig. 18. Signal power with 200 ms of coherent integration period.

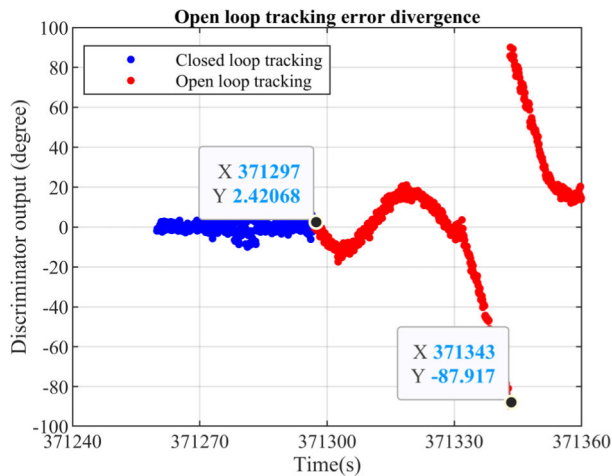


Fig. 19. Phase error divergence when the open loop tracking is adopted.

are less than four closed loop channels and the OL tracking duration is short enough to guarantee that the OL carrier phase error is small, the OL carrier phase observation can also be used in the positioning algorithm to improve the continuity of the positioning.

C. INS-Aided Cycle Slip Detection Validation and Performance

As mentioned in section II, the performance of the ordinary INS-aided cycle slip detection algorithm deteriorates severely

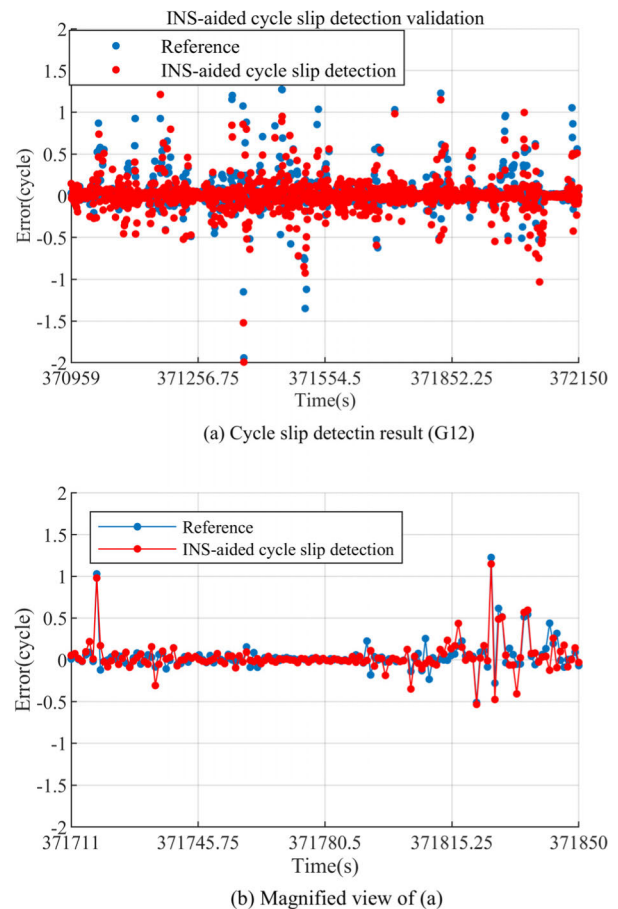


Fig. 20. Validation of the MEMS INS aided cycle slip detection.

when a MEMS IMU is used with a detection update rate of 1 Hz. In order to solve the problem, the accumulated cycle slip decision variable (ACSDV) is proposed. The effectiveness of the INS-aided cycle slip detection will be validated first.

The MEMS IMU ADIS 16465 is used to detect the cycle slips in the test. The detection rate is 20 Hz, which means 20 successive raw decision variables will be accumulated to generate the ACSDV within 1 second. Fig. 20 shows the reference phase errors and the ACSDVs by blue and red lines, respectively. The reference phase errors are derived by replacing the INS solution with the ground truth in the processing flow shown in Fig. 8. It is reasonable because the $\nabla\Delta r^{(i,k)}$ in (23) would be 0 if the ground truth is used, leaving only the cycle slips. Fig. 20 (a) is the overall comparison result, and (b) shows the magnified view of (a). Compared with the cycle slip results with 1 Hz detection rate shown in Fig. 11, the fluctuation caused by the INS error divergence is eliminated. The two curves in Fig. 20 are consistent with each other, indicating that the proposed accurate cycle slip detection using a MEMS IMU is effective.

Next, the performance improvement after adopting the INS-aided cycle slip detection and repairing algorithm will be evaluated. Due to the potential of long coherent integration to mitigate cycle slips, the integration period of 20 ms is selected within the INS-LCI architecture to investigate the specific performance of the INS-aided cycle slip detection algorithm.

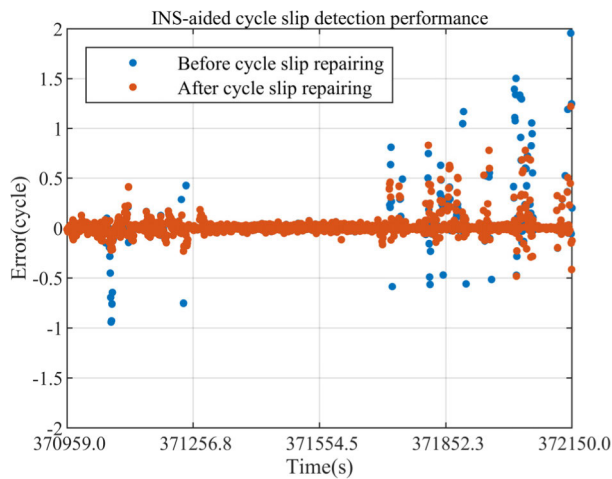


Fig. 21. Carrier phase errors before and after the cycle slip repairing.

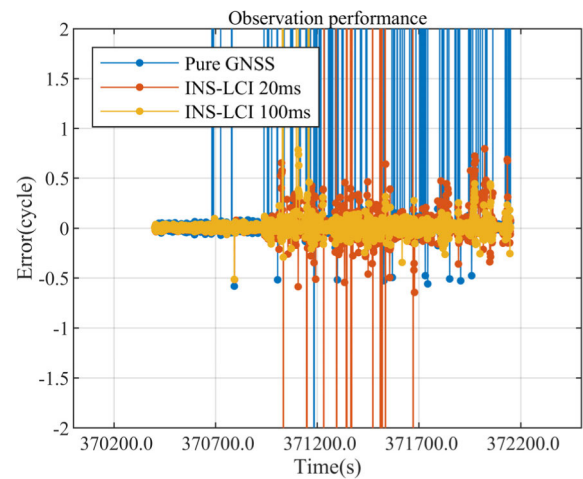


Fig. 22. Observation performance comparison.

TABLE II

PROPORTION OF EPOCHS WITH CYCLE SLIPS

PRN	Before cycle clip repairing	After cycle clip repairing
G32	3.60%	1.50%
G23	0.00%	0.00%
G18	0.60%	0.80%
G15	2.80%	1.70%
G12	7.50%	4.50%
G10	1.20%	1.30%

Fig. 21 shows the phase errors of satellite GPS 32 before and after the cycle slip repairing. It indicates that the INS-aided cycle slip detection and repairing algorithm can effectively reduce the cycle slips, providing more accurate and robust carrier phases.

Table II shows the proportion of epochs with cycle slips relative to the total number of epochs. The epochs with the detection decision variable larger than 0.45 cycles will be determined as cycle slips. Satellites GPS 32 and 12 have lower elevation angles, hence more cycle slips will happen. The INS-aided cycle slip detection and repairing algorithm works effectively especially in the scenarios where there are many cycle slips. A slight increase in the occurrence of cycle slips for GPS satellites 18 and 10 can be observed after the repairing process. It is attributed to the false detection caused by the MEMS INS error.

The MEMS INS-aided cycle slip detection algorithm effectively improves the carrier phases especially in severe conditions. The elevation angle can be used as an indicator to decide whether to repair the carrier phases.

D. INS-LCI Comprehensive Performance

The INS-LCI comprehensive performance test is conducted in this sub-section. The observations of Ublox F9P will be used as the benchmark of a pure GNSS receiver. The GNSS/INS

ultra-tight integration and multichannel cooperative loop in the INS-LCI architecture will be adopted to eliminate the effects of dynamic stress and oscillator instability. Accurate carrier phase open loop tracking guarantees the continuity of the observations. Besides, the INS-aided cycle slip detection improves the carrier phases at the observation level. Two coherent integration periods, 20 ms and 100 ms, will be tested to demonstrate the priority of the long coherent integration.

Fig. 22 displays the cycle slips of the satellite GPS 12 for pure GNSS, 20 ms INS-LCI and 100 ms INS-LCI. The long coherent integration has a significant carrier phase observation improvement in both accuracy and continuity. Almost all the phase errors are below 0.5 cycles.

The quantitative results of all the satellites are summarized in TABLE III. The maximum (MAX) and root mean square (RMS) values of the phase errors are evaluated to assess the accuracy. Besides, the valid epoch proportion is also calculated to assess the continuity of the carrier phases. In general, the INS-LCI 20 ms outperforms the pure GNSS and the INS-LCI 100 ms has the best performance. Although the carrier phase accuracy of satellites GPS 12, 15 and 32 in INS-LCI 20 ms is marginally lower compared to pure GNSS, the INS-LCI 20 ms exhibits a much higher proportion of valid epochs. It can be attributed to the accurate open loop tracking and the INS-aided cycle slip detection techniques. They improve the continuity of the carrier phase observations at the signal tracking and observation levels. In addition, the INS-LCI 100 ms presents the best performance in both accuracy and continuity. Take the satellite with the lowest elevation angle, GPS 12, as an example. The INS-LCI 100 ms achieves a comparable accuracy with pure GNSS but it improves the continuity by nearly 40%. And the INS-LCI 100 ms demonstrates varying degrees of improvement in the carrier phase accuracy of the other satellites. Compared with INS-LCI 20 ms, the INS-LCI 100 ms improves the carrier phase accuracy by 73.1% at most in terms of RMS. The results prove that the INS-LCI is capable of providing robust, accurate and continuous carrier phase observations.

TABLE III
CARRIER PHASE ERRORS OF DIFFERENT SOLUTIONS

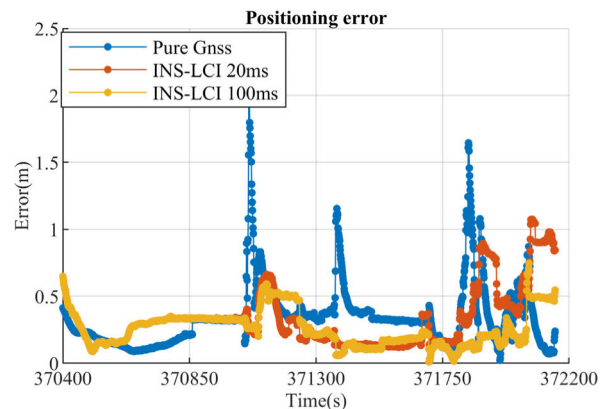
PRN	Solution	MAX (cycle)	RMS (cycle)	Valid Epochs (%)
G10	Pure GNSS	17.009	0.529	95.00%
	INS-LCI 20 ms	0.852	0.156	99.20%
	INS-LCI 100 ms	0.588	0.042	99.30%
G12	Pure GNSS	0.193	0.063	59.00%
	INS-LCI 20 ms	0.796	0.117	97.30%
	INS-LCI 100 ms	0.784	0.072	99.10%
G15	Pure GNSS	2.41	0.075	93.50%
	INS-LCI 20 ms	1.352	0.102	98.90%
	INS-LCI 100 ms	0.519	0.042	99.00%
G18	Pure GNSS	6.011	0.156	98.70%
	INS-LCI 20 ms	1.145	0.076	99.90%
	INS-LCI 100 ms	0.437	0.026	100.00%
G32	Pure GNSS	0.294	0.042	89.90%
	INS-LCI 20 ms	1.22	0.096	99.90%
	INS-LCI 100 ms	0.266	0.037	100.00%

TABLE IV
POSITIONING ERRORS OF DIFFERENT SOLUTIONS

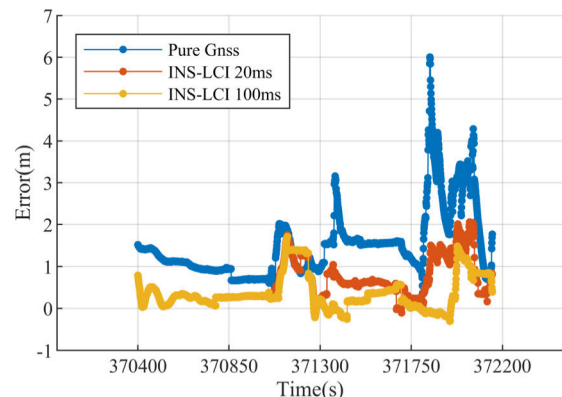
	Solution	Max (m)	RMS (m)	Cep95 (m)
Horizontal	Pure GNSS	2.107	0.422	0.812
	INS-LCI 20ms	1.075	0.393	0.874
	INS-LCI 100ms	0.745	0.292	0.509
Vertical	Pure GNSS	6.006	1.714	3.296
	INS-LCI 20ms	2.058	0.741	1.544
	INS-LCI 100ms	1.711	0.55	1.378

The observations of pure GNSS, INS-LCI 20ms and INS-LCI 100 ms are then processed by PLANSofT™, a RTK processing engine developed by Position, Location And Navigation (PLAN) Group, University of Calgary [41]. GPS L1 observations and a long baseline are used. The horizontal and vertical positioning errors are shown in Fig. 23, and the statistical results of the errors are listed in TABLE IV.

Due to the long baseline and the fact that only the single frequency carrier phase observations of seven GPS satellites (four of them have low elevation angles) are used in the RTK solution, the positioning errors are decimeter accurate. Nevertheless, the results demonstrate that the INS-LCI architecture can improve the positioning accuracy significantly in challenging environments. The pure GNSS has the worst performance. Compared with the INS-LCI 20 ms, the INS-LCI 100 ms improves the horizontal and vertical positioning accuracy by 41.8% and 10.8% respectively in terms of Cep95,



(a) Horizontal positioning error



(b) Vertical positioning error

Fig. 23. Positioning performance comparison.

validating the superiority of the long coherent integration. The fixing rates of the pure GNSS, INS-LCI 20 ms and INS-LCI 100 ms are 42.5%, 56.9% and 72.0%, respectively, which indicates the INS-LCI can provide more accurate and robust carrier phase observations and positioning.

V. CONCLUSION

We have introduced a MEMS INS aided long coherent integration GNSS receiver architecture. The pre-requisite of effective long coherent integration is that the phase error during an integration period should be as “white” as possible. Therefore, a MEMS INS/GNSS ultra-tight integration is developed to eliminate the effects due to the receiver-satellite relative dynamics. In addition, a multichannel cooperative loop is proposed to track and compensate for the local oscillator instability. In order to improve the continuity of the long coherent tracking, an open loop tracking strategy is implemented to sustain the integer ambiguity when the signal is blocked. Finally, a MEMS INS aided cycle slip detection algorithm is developed to further improve the quality of the carrier phases.

All these techniques have been implemented in our software-defined multi-sensor GNSS receiver, I2xSNR. Field tests demonstrate that the long coherent architecture is capable of restricting the carrier phase error below 0.5 cycles with a

superior continuity performance in harsh environments. The RTK positioning result also proves its superiority.

In the future, multi-sensor fusion will be conducted to improve the INS-LCI architecture further. A vision sensor, such as a camera, will be used to assist the tracking state switching, and to monitor the distribution of the satellites, etc. The robust and accurate carrier phase measurement in extreme complex urban areas will be explored.

ACKNOWLEDGMENT

The algorithm is implemented by the Integrated and Intelligent Navigation (I2Nav) Group, GNSS Research Center, Wuhan University. Tisheng Zhang, Xin Feng, and Xiaoji Niu would like to thank Mohamed Bochkati and Thomas Pany who are with Universität der Bundeswehr München.

REFERENCES

- [1] N. Zhu, J. Marais, D. Betaille, and M. Berbineau, "GNSS position integrity in urban environments: A review of literature," *IEEE Trans. Intell. Transp. Syst.*, vol. 19, no. 9, pp. 2762–2778, Sep. 2018.
- [2] D. Lu and E. Schnieder, "Performance evaluation of GNSS for train localization," *IEEE Trans. Intell. Transp. Syst.*, vol. 16, no. 2, pp. 1054–1059, Apr. 2015.
- [3] S. Kuutti, S. Fallah, K. Katsaros, M. Dianati, F. McCullough, and A. Mouzakitis, "A survey of the state-of-the-art localization techniques and their potentials for autonomous vehicle applications," *IEEE Internet Things J.*, vol. 5, no. 2, pp. 829–846, Apr. 2018.
- [4] T. Li, H. Zhang, Z. Gao, Q. Chen, and X. Niu, "High-accuracy positioning in urban environments using single-frequency multi-GNSS RTK/MEMS-IMU integration," *Remote Sens.*, vol. 10, no. 2, p. 205, Jan. 2018.
- [5] T. E. Humphreys, M. J. Murrian, and L. Narula, "Deep-urban unaided precise global navigation satellite system vehicle positioning," *IEEE Intell. Transp. Syst. Mag.*, vol. 12, no. 3, pp. 109–122, Jun. 2020.
- [6] T. Pany et al., "Coherent integration time: The longer, the better," *Inside GNSS*, vol. 4, pp. 52–61, Aug. 2009.
- [7] A. Shafaati, T. Lin, and G. Lachapelle, "Performance comparison of difference correlator and co-op tracking architectures under receiver clock instability," in *Proc. 28th Int. Tech. Meeting Satell. Division The Inst. Navigat.*, 2015, pp. 2887–2904.
- [8] R. Watson, M. Petovello, G. Lachapelle, and R. Klukas, "Impact of oscillator errors on IMU-aided GPS tracking loop performance," in *Proc. Eur. Navigat. Conf.*, 2007, p. 115.
- [9] E. Rebeyrol, O. Julien, C. Macabiau, L. Ries, A. Delatour, and L. Lestarquit, "Galileo civil signal modulations," *GPS Solutions*, vol. 11, no. 3, pp. 159–171, Jul. 2007.
- [10] F. Van Diggelen, *A-GPS: Assisted GPS, GNSS, and SBAS*. Norwood, MA, USA: Artech House, 2009.
- [11] T. Ren and M. G. Petovello, "A stand-alone approach for high-sensitivity GNSS receivers in signal-challenged environment," *IEEE Trans. Aerosp. Electron. Syst.*, vol. 53, no. 5, pp. 2438–2448, Oct. 2017.
- [12] T. Pany, H. Euler, and J. Winkel, "Indoor carrier phase tracking and positioning with difference correlators," in *Proc. 24th Int. Tech. Meeting Satell. Division Inst. Navigat.*, 2011, pp. 2202–2213.
- [13] S. Chen, Y. Gao, and T. Lin, "Effect and mitigation of oscillator vibration-induced phase noise on carrier phase tracking," *GPS Solutions*, vol. 21, no. 4, pp. 1515–1524, Oct. 2017.
- [14] S. Bhaskar, J. T. Curran, and G. Lachapelle, "Improving GNSS carrier-phase tracking via oscillator g-sensitivity compensation," *IEEE Trans. Aerosp. Electron. Syst.*, vol. 51, no. 4, pp. 2641–2654, Oct. 2015.
- [15] X. Feng, T. Zhang, X. Niu, T. Pany, and J. Liu, "Improving GNSS carrier phase tracking using a long coherent integration architecture," *GPS Solutions*, vol. 27, no. 1, p. 37, Jan. 2023.
- [16] Y. Ban, X. Niu, T. Zhang, Q. Zhang, and J. Liu, "Modeling and quantitative analysis of GNSS/INS deep integration tracking loops in high dynamics," *Micromachines*, vol. 8, no. 9, p. 272, Sep. 2017.
- [17] T. Zhang, Y. Ban, X. Niu, W. Guo, and J. Liu, "Improving the design of MEMS INS-aided PLLs for GNSS carrier phase measurement under high dynamics," *Micromachines*, vol. 8, no. 5, p. 135, Apr. 2017.
- [18] T. Pany et al., "Performance of a partially coherent ultra-tightly coupled GNSS/INS pedestrian navigation system enabling coherent integration times of several seconds to track GNSS signals down to 1.5 dBHz," in *Proc. 22nd Int. Tech. Meeting Satell. Division Inst. Navigat. (ION GNSS 2009)*, 2009, pp. 919–934.
- [19] A. Soloviev and J. Dickman, "Extending GPS carrier phase availability indoors with a deeply integrated receiver architecture," *IEEE Wireless Commun.*, vol. 18, no. 2, pp. 36–44, Apr. 2011.
- [20] R. Watson, G. Lachapelle, and R. Klukas, "Testing oscillator stability as a limiting factor in extreme high-sensitivity GPS applications," in *Proc. Eur. Navigat. Conf.*, 2006, pp. 1–24.
- [21] P. O. Gaggero and D. Borio, "Ultra-stable oscillators: Limits of GNSS coherent integration," in *Proc. 21st Int. Tech. Meeting Satell. Division Inst. Navigat.*, 2008, pp. 565–575.
- [22] *ZED-F9K-00B, High Precision Automotive DR GNSS Receiver Professional Grad*, document UBX-17061422-R07, 2023.
- [23] *MicroStrain 3DM-GQ7-GNSS/INS Tactical Grade RTK-Enabled Navigation System*, document 8400-0137, 8400.
- [24] P. Fan, X. Cui, S. Zhao, G. Liu, and M. Lu, "A two-step stochastic hybrid estimation for GNSS carrier phase tracking in urban environments," *IEEE Trans. Instrum. Meas.*, vol. 70, pp. 1–18, 2021.
- [25] F. van Graas, A. Soloviev, M. Uijt de Haag, and S. Gunawardena, "Closed-loop sequential signal processing and open-loop batch processing approaches for GNSS receiver design," *IEEE J. Sel. Topics Signal Process.*, vol. 3, no. 4, pp. 571–586, Aug. 2009.
- [26] G. Stienne, S. Reboul, M. Azmani, J. B. Choquel, and M. Benjelloun, "GNSS dataless signal tracking with a delay semi-open loop and a phase open loop," *Signal Process.*, vol. 93, no. 5, pp. 1192–1209, May 2013.
- [27] H. Lin, X. Tang, and G. Ou, "An open loop with Kalman filter for intermittent GNSS signal tracking," *IEEE Commun. Lett.*, vol. 21, no. 12, pp. 2634–2637, Dec. 2017.
- [28] Z. Li, T. Zhang, F. Qi, H. Tang, and X. Niu, "Carrier phase prediction method for GNSS precise positioning in challenging environment," *Adv. Space Res.*, vol. 63, no. 7, pp. 2164–2174, Apr. 2019.
- [29] A. Lipp and X. Gu, "Cycle-slip detection and repair in integrated navigation systems," in *Proc. IEEE Position, Location Navigat. Symp.*, Aug. 1994, pp. 681–688.
- [30] H.-K. Lee, J. Wang, and C. Rizos, "Effective cycle slip detection and identification for high precision GPS/INS integrated systems," *J. Navigat.*, vol. 56, no. 3, pp. 475–486, Sep. 2003.
- [31] L. Huang et al., "A new triple-frequency cycle slip detecting algorithm validated with BDS data," *GPS Solutions*, vol. 20, no. 4, pp. 761–769, Oct. 2016.
- [32] S. Du and Y. Gao, "Inertial aided cycle slip detection and identification for integrated PPP GPS and INS," *Sensors*, vol. 12, no. 11, pp. 14344–14362, Oct. 2012.
- [33] T. Takasu and A. Yasuda, "Cycle slip detection and fixing by MEMS-IMU/GPS integration for mobile environment RTK-GPS," in *Proc. 21st Int. Tech. Meeting Satell. Division Inst. Navigat.*, 2008, pp. 64–71.
- [34] J. Dampf, M. Bochkati, and T. Pany, "Towards single antenna phase-coherent INS-beamforming to enable RTK with low-end antennas," in *Proc. Int. Tech. Meeting Satell. Division Inst. Navigat.*, Oct. 2022, pp. 2202–2214.
- [35] M. Bochkati, J. Dampf, and T. Pany, "Receiver clock estimation for RTK-grade multi-GNSS multi-frequency synthetic aperture processing," in *Proc. IEEE/ION Position, Location Navigat. Symp. (PLANS)*, Apr. 2023, pp. 968–976.
- [36] X. Niu, Y. Ban, Q. Zhang, T. Zhang, H. Zhang, and J. Liu, "Quantitative analysis to the impacts of IMU quality in GPS/INS deep integration," *Micromachines*, vol. 6, no. 8, pp. 1082–1099, Aug. 2015.
- [37] B. K. H. Soon, S. Scheduling, H.-K. Lee, H.-K. Lee, and H. Durrant-Whyte, "An approach to aid INS using time-differenced GPS carrier phase (TDGP) measurements," *GPS Solutions*, vol. 12, no. 4, pp. 261–271, Sep. 2008.
- [38] C. Altmayer, "Enhancing the integrity of integrated GPS/INS systems by cycle slip detection and correction," in *Proc. IEEE Intell. Vehicles Symp.*, Jul. 2000, pp. 174–179.
- [39] *Spirent GSS6450 Multi-frequency Record & Playback System*, document MS3098, 2022.
- [40] *ZED-F9P-04B High Precision GNSS Module Professional Grade*, document UBX-21044850, 2021.
- [41] R. Ong, "Reliability of combined GPS/GLONASS ambiguity resolution," in *Proc. Masters Abstracts Int.*, vol. 49, no. 3, Jul. 2010.



Tisheng Zhang received the B.Sc. and Ph.D. degrees in communication and information systems from Wuhan University, Wuhan, China, in 2008 and 2013, respectively. From 2018 to 2019, he was a Post-Doctoral Researcher with The Hong Kong Polytechnic University. He is currently an Associate Professor with the GNSS Research Center, Wuhan University. His research interests include GNSS receivers, multi-sensor deep integration, and robot navigation.



Mohamed Bochkati received the bachelor's and master's degrees in geodesy and geoinformation from the Technical University of Munich. He is currently a Research Associate with the Institute of Space Technology and Space Applications (ISTA), Universität der Bundeswehr München. His research interests include deeply coupled GNSS/INS integration and novel calibration techniques for MEMS-IMUs.



Xin Feng received the B.E. and M.E. degrees from Wuhan University, Wuhan, China, in 2018 and 2021, respectively, where he is currently pursuing the Ph.D. degree in geodesy and survey engineering with the School of Geodesy and Geomatics. His primary research interests include GNSS receiver and multi-sensor ultra-tightly integrations.



Thomas Pany (Senior Member, IEEE) is currently a Full Professor with the Faculty of Aerospace Engineering, Universität der Bundeswehr München, where he teaches satellite navigation. He has around 200 publications, including patents and one monography. His research interests include GNSS/LTE/5G signal design and processing, software receivers, and GNSS/INS/LiDAR fusion.



Xiaoji Niu is currently a Professor with the GNSS Research Center, Wuhan University, China. He has published more than 90 academic articles and owns 28 patents. He leads a multi-sensor navigation group focusing on GNSS/INS integration, low-cost navigation sensor fusion, and its new applications.



Jingnan Liu is currently a member of the Chinese Academy of Engineering, a Professor, and a Ph.D. Supervisor. He is also an Expert in geodesy and surveying engineering with a specialty in GNSS technology and applications. He has been engaged in the research of geodetic theories and applications, including national coordinate systems, GNSS technology, and software development, as well as large project implementations.